RESEARCH PAPER

# Pore-Engineered Mesoporous Reduced Graphene Oxide for Fast Energy Storage in Supercapacitors

**Neha Rani[1], Jayati Chatterjee Mitra[1*]**
Department of Chemistry, Dr. C.V. Raman University, Kota, Bilaspur (C.G).
*Corresponding author Email: mailto:jayatimitra@cvru.ac.inneharani121088@gmail.com

**Abstract**
Restacking of graphene nanosheets collapses the electrolyte-accessible surface and lengthens ion pathways, which limits the capacitance and rate capability of graphene-based electrical double-layer capacitors (EDLCs). Here we report mesoporous reduced graphene oxide (m-rGO) with a narrow pore-size distribution centred at 3.5 nm, made by CTAB-directed assembly of a mesoporous silica layer on graphene oxide, carbonization with KOH activation, and HF removal of the silica. The material has an apparent BET surface area of 2684 $m^2 g^{-1}$, a pore volume of 1.92 $cm^3 g^{-1}$, a mesopore fraction of 78.4% and an electrical conductivity of 628 S $m^{-1}$. In symmetric coin cells with neat [EMIM][$BF_4$] over 0–3.5 V it delivers 286 F $g^{-1}$ at 1 A $g^{-1}$ and keeps 212 F $g^{-1}$ at 50 A $g^{-1}$ (74.1%). The calculated cell energy density is 122 Wh $kg^{-1}$ at 0.88 kW $kg^{-1}$ (118 Wh $kg^{-1}$ with the measured IR drop subtracted), and capacitance retention is 96.4% after 20,000 cycles. The impedance relaxation time is 145 ms, against 4820 ms for restacked rGO. Among samples with mean pore sizes of 2.1, 3.5 and 5.4 nm, capacitance is highest at 3.5 nm, although area and conductivity change together with pore size. A second route using a block-copolymer template and CVD gives MG-3.8 (3.8 nm pores, 1285 $m^2 g^{-1}$), which delivers 312 F $g^{-1}$ at 0.5 A $g^{-1}$ in 6 M KOH and keeps 94.8% of its capacitance over 10,000 cycles. In both series the mesoporous sample outperforms its non-porous reference.

**Keywords:** mesoporous graphene; reduced graphene oxide; pore engineering; supercapacitor; ionic liquid; electrical double-layer capacitance
**How to cite this article:** Neha Rani1 Jayati Chatterjee Mitra1*. Pore-Engineered Mesoporous Reduced Graphene Oxide for Fast Energy Storage in Supercapacitors. Int J Drug Deliv Technol. 2026;16(89s):1472-1488. DOI: 10.25258/ijddt.16.89s.155.

## 1. Introduction

Electrical double-layer capacitors (EDLCs) store charge by electrosorption of electrolyte ions at the electrode surface and fill the gap in power and energy between dielectric capacitors and batteries [1–3]. Their capacitance and rate response depend on the electrolyte-accessible surface area, the pore-size distribution relative to the ion size, the interfacial resistance and the electronic conductivity of the electrode [3–7]. Reviews of carbon–electrolyte pairings show that EDLC energy density is limited both by the cell voltage and by the fraction of the carbon surface that ions can actually reach [8–11].

Graphene combines a theoretical surface area of 2630 $m^2 g^{-1}$ with high carrier mobility, a thermal conductivity in the kW $m^{-1} K^{-1}$ range for suspended monolayers and a Young's modulus near 1 TPa, and these properties have driven work on composites and devices [12–17]. Sheets processed from solution, however, restack through π–π and van der Waals interactions during filtration and drying. The accessible area of reduced graphene oxide (rGO) films then falls to a few hundred $m^2 g^{-1}$ and the sheets form tortuous diffusion paths [18–21]. Early graphene supercapacitors gave modest capacitance for this reason [13, 22], and activation or spacers were needed to keep the area open [23, 24]. Chemically derived graphene is usually obtained through graphene oxide (GO) and its reduction [25–29]. GO is a non-stoichiometric sheet carrying epoxide, hydroxyl and carboxyl groups [30–33]. Reduction removes most of these groups but leaves vacancy defects and residual oxygen [34–36], and the conductivity of the product rises by orders of magnitude as the $sp^2$ network is restored [37–40]. The same oxygen groups make GO dispersible in water [41–43] and available for covalent or electrostatic modification [44], which allows films and electrodes to be assembled from solution [38, 40, 45]. We use the negative surface charge of GO to anchor a cationic surfactant template.

Pore size relative to ion size controls double-layer capacitance. Anomalous capacitance gains in sub-nanometre carbon pores [46], the matching of ion and pore size [47], the effect of pore-size dispersity [48], and the effects of ion size and electrode curvature in ionic liquids [49–51] are all established for carbons. Molecular simulation and theory show how ions pack and screen charge inside nanopores [52, 53]. Micropores raise capacitance at low rates, but in viscous organic and ionic-liquid electrolytes ions meet steric and transport limits inside them [54]. Ionic liquids such as 1-ethyl-3-methylimidazolium tetrafluoroborate ([EMIM][$BF_4$]) extend the voltage window beyond 3.5 V [55]. Because energy scales with the square of the voltage, a 3.5 V window gives roughly 12 times the energy of a 1.0 V aqueous cell, or 4.8 times that of a 1.6 V cell, at equal capacitance. The ions are about 0.76 × 0.43 nm ($[EMIM]^+$) and 0.45 nm ($[BF_4]^-$) [47, 48], so a pair of them needs pores that are open enough to carry viscous flow.

Mesopores (2–50 nm) keep a large surface and open transport channels. KOH activation of graphene gives very high area but mostly micropores [23]. Template routes have a long record in mesoporous silica and carbon: liquid-crystal templating produced the M41S silicas [56, 57], block copolymers widened the pores to 5–30 nm [58, 59], and carbon replicas of silica followed [60, 61]. The TEOS coating used here follows the base-catalysed Stöber route [62]. Reviews of mesoporous and porous carbons summarise these methods [63, 64]. The same ideas were later applied to

graphene: mesoporous carbon spheres were intercalated between rGO sheets [65], holey graphene frameworks were prepared [66], and restacking was suppressed by liquid-mediated or bioinspired assembly [19, 21].

A second strategy builds three-dimensional graphene networks that hold the sheets apart: hydrogels [67, 68] and macro/mesoporous frameworks [69, 70]. Graphene has also been combined with $MnO_2$ to add pseudocapacitance [71–73], and doped with nitrogen or boron [74–77]. Routes to doped graphene include annealing with melamine [78], electrothermal reaction with ammonia [79] and several others [80–84], and single dopant sites have been imaged [85, 86]. Nitrogen-doped mesoporous carbon has reached very high capacitance [87]. The present work concerns double-layer storage only.

To our knowledge, few reports pair a uniform 3–4 nm pore size with a high-voltage ionic-liquid electrolyte, and the pore size that suits [EMIM][$BF_4$] has not been mapped across a series with otherwise similar chemistry. Onion-like carbon showed an ultrahigh-power route [88], carbide-derived carbon films have been integrated on silicon chips [89], and curved graphene sheets that resist restacking have delivered high energy density in an ionic liquid [90], but none combines a graphene-based electrode with a controlled mesopore size. Here we (i) prepare mesoporous rGO (m-rGO) with mean pore diameters of 2.1, 3.5 and 5.4 nm by CTAB-directed silica templating; (ii) relate pore size, surface chemistry and conductivity to capacitance, rate capability and impedance in neat [EMIM][$BF_4$]; and (iii) test whether the same principle holds for a second, block-copolymer and chemical-vapour-deposition route (MG-3.8) evaluated in aqueous KOH.

## 2. Experimental Section

### *2.1 Reagents and Materials*

Natural graphite flakes (99.8% carbon basis, 325 mesh), cetyltrimethylammonium bromide (CTAB, ≥99.0%), tetraethyl orthosilicate (TEOS, 98%), potassium hydroxide (KOH, ≥90%), hydrofluoric acid (HF, 48 wt.% in water), polytetrafluoroethylene (PTFE, 60 wt.% aqueous suspension), carbon black (Super P) and [EMIM][$BF_4$] (electrochemical grade, ≥99.0%) were purchased from Sigma-Aldrich. Sulfuric acid (98%), phosphoric acid (85%), potassium permanganate (99.5%), hydrogen peroxide (30% v/v) and absolute ethanol (99.9%) were obtained from HiMedia Laboratories. All aqueous solutions used deionized water (≥18.2 MΩ cm at 25 °C) from a Millipore Milli-Q system.

For the block-copolymer route, poly(styrene)-block-poly(2-vinylpyridine) (PS-b-P2VP, Mn = 55,000-b-12,000 g $mol^{-1}$) was obtained from Polymer Source Inc. (Dorval, Canada). Sodium nitrate and hydrochloric acid (37%) were of analytical grade from HiMedia Laboratories or Merck. Acetylene (99.9%) and argon (99.999%) were supplied by local industrial suppliers. All reagents were used as received.

### *2.2 Synthesis of Graphene Oxide*

GO for the m-rGO series was prepared from natural graphite by the improved Hummers method [25, 26]. $H_2SO_4$ (360 mL) and $H_3PO_4$ (40 mL; 9:1 v/v) were chilled to 0 °C, and graphite (3.0 g) was added under mechanical stirring at 400 rpm. $KMnO_4$ (18.0 g) was added slowly so that the temperature stayed below 20 °C. The slurry was heated to 50 °C and stirred for 12 h, then poured onto 400 g of crushed ice containing 3 mL of 30% $H_2O_2$. The product was washed by repeated centrifugation (10,000 rpm, 20 min, Hermle Z326K) with 5% HCl and then with water until the supernatant reached pH 6.8. The GO was redispersed and exfoliated by probe sonication (Sonics Vibra-Cell VCX 750, 40% amplitude, 20 kHz, 60 min, 5 s on / 2 s off, ice-water cooling). Unexfoliated debris was removed at 4,000 rpm for 30 min, which gave a stable aqueous GO suspension at 2.0 mg $mL^{-1}$.

GO for the MG-3.8 series was prepared by a modified Hummers method. Graphite (2.0 g) was dispersed in 50 mL of concentrated $H_2SO_4$ at 0 °C, and $NaNO_3$ (1.0 g) and $KMnO_4$ (6.0 g) were added gradually. After 2 h the temperature was raised to 35 °C for 30 min, 100 mL of water was added carefully, and the mixture was heated to 95 °C for 15 min. The reaction was stopped with 300 mL of water and 10 mL of $H_2O_2$. The GO was washed to neutral pH and freeze-dried.

### *2.3 Synthesis of m-rGO by CTAB-Directed Silica Templating*

The m-rGO series was made by a dual soft-template / hard-mask sacrificial route; the sequence is shown in Figure 1 and the conditions for every sample are listed in Table 1.

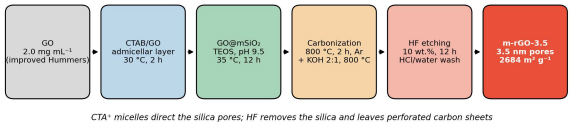



**Figure 1.** Synthesis sequence of m-rGO-3.5: GO is complexed with CTAB, coated with mesoporous silica, carbonized and activated, and finally etched with HF.

*CTAB–GO complexation.* GO dispersion (200 mL, 2.0 mg $mL^{-1}$, i.e. 400 mg GO) was diluted with 200 mL of water and 100 mL of ethanol. CTAB (1.50 g) was added slowly and stirred at 30 °C for 2 h. Electrostatic attraction between the $CTA^+$ headgroups and the carboxyl and hydroxyl groups on GO drove assembly of an admicellar surfactant layer on the basal plane [56, 57].

*Mesoporous silica coating.* Aqueous ammonia (2.5 mL, 28 wt.%) raised the pH to 9.5. TEOS (3.20 mL in 20 mL of ethanol) was added with a syringe pump at 0.2 mL $min^{-1}$ under vigorous agitation. Hydrolysis and co-condensation across the $CTA^+$ micelles proceeded for 12 h at 35 °C and is expected to give a sandwich-structured GO@$mSiO_2$ intermediate; this structure was not verified by microscopy in the present work. The ammonia-catalysed hydrolysis of TEOS in ethanol follows the Stöber route [62].

*Carbonization and activation.* The composite was filtered, washed with ethanol, dried at 70 °C for 12 h and heated in an alumina tube furnace (Nabertherm RHTC 80-230/15) under argon (99.999%, 100 mL $min^{-1}$; 60 min purge). The temperature was raised to 800 °C at 5 °C $min^{-1}$ and held for 2 h. For KOH activation the carbonized intermediate was

impregnated with aqueous KOH (KOH:C = 2:1 by mass), dried at 110 °C and annealed at 800 °C for 1 h under argon.

*Template removal.* The silica was etched in 10 wt.% HF at room temperature for 12 h. The carbon was washed with 1 M HCl and hot water (80 °C) to neutral pH and dried under vacuum at 100 °C for 24 h, which gave m-rGO-3.5. Comparative samples with mean pore diameters of 2.1 nm (m-rGO-2.1) and 5.4 nm (m-rGO-5.4) were made by adjusting the TEOS/surfactant ratio and the activation temperature (700, 800 and 900 °C). Non-porous reference rGO was made by thermal reduction of GO under the same furnace conditions without CTAB or TEOS.

### *2.4 Synthesis of MG-3.8 by Block-Copolymer Templating and CVD*

GO (200 mg) was dispersed in 40 mL of ethanol containing 80 mg of PS-b-P2VP and stirred for 12 h. The mixture was transferred to a porcelain boat and dried at 60 °C. The solid was treated by chemical vapour deposition under Ar/$C_2H_2$ (100:10 sccm) at 900 °C for 30 min and annealed at 1000 °C for 1 h under pure argon. After cooling, it was washed with dilute HCl and hot ethanol to remove residual template fragments, which gave MG-3.8. Two controls were prepared under otherwise identical conditions: template-free reduced GO (rGO) and chemically etched graphene with disordered pores (EG).

**Table 1.** Preparation conditions of all samples.

| Sample | Route | Structure-directing agent | Thermal / chemical treatment | Mean pore (nm) |
|---|---|---|---|---|
| Pristine rGO | Thermal reduction of GO | None | Furnace conditions identical to m-rGO series; no CTAB or TEOS | 1.8 |
| m-rGO-2.1 | CTAB/TEOS, silica template | CTAB and TEOS, ratio adjusted | Carbonization and activation at a temperature in the 700–900 °C range; HF etching | 2.1 |
| **m-rGO-3.5** | **CTAB/TEOS, silica template** | **CTAB 1.50 g, TEOS 3.20 mL per 400 mg GO (CTAB:GO = 3.75:1 by mass; TEOS:CTAB ≈ 3.5:1 by mole)[a]** | **800 °C, 2 h under Ar; KOH:C = 2:1, 800 °C, 1 h; HF etching** | **3.5** |
| m-rGO-5.4 | CTAB/TEOS, silica template | CTAB and TEOS, ratio adjusted | Carbonization and activation at a temperature in the 700–900 °C range; HF etching | 5.4 |
| MG-3.8 | Block-copolymer template, CVD | PS-b-P2VP, 80 mg per 200 mg GO (0.4:1 by mass) | Ar/$C_2H_2$ 100:10 sccm, 900 °C, 30 min; anneal 1000 °C, 1 h, Ar; HCl/ethanol wash | 3.8 |
| rGO (control, MG route) | Template-free | None | As MG-3.8, no PS-b-P2VP | — |
| EG (control) | Chemical etching | None | Chemically etched graphene, otherwise identical conditions | 2–12 (broad) |

[a] Calculated from the quantities given, using M(CTAB) = 364.45 g mol$^{-1}$, M(TEOS) = 208.33 g mol$^{-1}$ and ρ(TEOS) = 0.933 g mL$^{-1}$: 4.1 mmol CTAB and 14.3 mmol TEOS. The two comparison m-rGO samples differ from m-rGO-3.5 in TEOS/surfactant ratio and activation temperature; the individual values were not recorded for each sample. Pore sizes are NLDFT (m-rGO series) or BJH (MG series) maxima.

### *2.5 Structural and Physicochemical Characterization*

The techniques and instruments are summarised in Table 2. Surface area was calculated by the multipoint Brunauer–Emmett–Teller (BET) method [91] over 0.05 < $P/P_0$ < 0.25. Pore-size distributions of the m-rGO series were derived by non-local density functional theory (NLDFT) with slit/cylindrical carbon pore models, and that of MG-3.8 from the adsorption branch by the Barrett–Joyner–Halenda (BJH) method [92]; the two methods give different absolute pore sizes and should not be compared directly. NLDFT kernels follow the methods reviewed in [93]. Isotherms were classified and reported following IUPAC recommendations [94–96]. Raman bands were interpreted following the established analyses of disordered carbon and graphene [97–101]. Samples were degassed at 200 °C for 12 h before sorption measurements.

**Table 2.** Characterization techniques and instrument settings.

| Technique | m-rGO series (ionic liquid) | MG-3.8 series (aqueous) | Key parameters |
|---|---|---|---|
| FE-SEM | JEOL JSM-7600F, 10 kV | Zeiss Gemini 300, 5 kV | Secondary-electron imaging |
| XRD | Bruker D8 Advance, Cu Kα | — | λ = 0.15418 nm; 2θ = 5–80°; 2° min⁻¹ |
| $N_2$ physisorption | Micromeritics ASAP 2420, 77.3 K | Micromeritics ASAP 2020, 77 K | Degas 200 °C, 12 h; BET 0.05–0.25 $P/P_0$ |
| Raman | Horiba LabRAM HR Evolution | Horiba LabRAM HR Evolution | 532 nm laser |
| XPS | Thermo Scientific K-Alpha | Thermo Scientific K-Alpha | Al Kα, hν = 1486.6 eV; C 1s at 284.8 eV |
| Electrical conductivity | Keithley 2450 SourceMeter | — | Four-probe, pressed discs |
| Electrochemistry | BioLogic VMP-3 | CHI 760E | See Sections 2.6 and 2.7 |

### *2.6 Electrochemical Measurements in Ionic Liquid*

Electrodes of the m-rGO series contained 85 wt.% active material, 10 wt.% Super P carbon black and 5 wt.% PTFE binder in ethanol. The paste was rolled into sheets, punched into discs and dried at 120 °C under vacuum for 12 h; the mass loading was 2.2 ± 0.1 mg $cm^{-2}$. Photographs of the powder, the electrode film and discs, and the coin-cell parts are shown in Figure 2. Symmetric CR2032 coin cells were assembled in an argon glove box (MBraun LABstar, $H_2O$ < 0.1 ppm, $O_2$ < 0.1 ppm) with neat [EMIM][$BF_4$], a Whatman GF/D glass-fibre separator, a stainless-steel spacer and a spring (components in Figure 2). Cyclic voltammetry (CV, 5–200 mV $s^{-1}$), galvanostatic charge–discharge (GCD, 0.5–50 A $g^{-1}$) between 0.0 and 3.5 V, and electrochemical impedance spectroscopy (EIS, 100 kHz–10 mHz, 10 mV amplitude at open-circuit potential) were run on a BioLogic VMP-3. Values are means ± standard deviation of three cells. Current densities are expressed per gram of active material in one electrode.

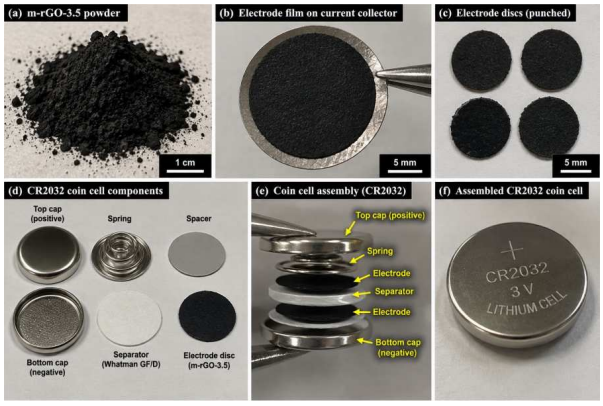



**Figure 2.** Experimental setup for the ionic-liquid cells: (a) m-rGO-3.5 powder, (b) electrode film on the current collector, (c) punched electrode discs, (d) CR2032 coin-cell components, (e) assembly order and (f) assembled coin cell.

The gravimetric capacitance of a single electrode ($C_s$), the cell energy density ($E_{cell}$) and the cell power density ($P_{cell}$) were calculated from GCD discharge curves:

$$C_s = 4\, I\, \Delta t / (m\, \Delta V)$$

$$E_{cell} = (1/8)\, C_s\, (\Delta V)^2 \times (100$$

$$P_{cell} = \Delta V\, j / 4$$

where I is the discharge current (A), Δt the discharge time (s), ΔV the discharge voltage window (V), m the total active mass of both electrodes (g), and j the current density per electrode mass (A $g^{-1}$); $C_s/4$ is the cell capacitance per total mass. $E_{cell}$ is in Wh $kg^{-1}$ and $P_{cell}$ in kW $kg^{-1}$ (per total electrode mass). Unless stated, ΔV is the full 3.5 V window, which gives an upper bound; where the IR drop was measured it is subtracted and this is stated. The EIS relaxation time constant is $\tau_0 = 1/f_0$, where $f_0$ is the frequency at which the phase angle reaches −45°:

$$\tau_0 = 1 / f_0$$

To compare materials of different area, the capacitance was also normalised to the BET area:

$$C_A = C_s / S_{BET}$$

### *2.7 Electrochemical Measurements in Aqueous Electrolyte*

Electrodes of the MG-3.8 series contained 90 wt.% active material and 10 wt.% PTFE in ethanol, rolled into thin films and pressed onto nickel foam (1 $cm^2$, mass loading ≈ 2.0 mg $cm^{-2}$). Measurements used a CHI 760E workstation in a three-electrode cell with 6 M KOH, a platinum counter electrode and an Ag/AgCl reference. CV (5–100 mV $s^{-1}$), GCD (0.5–20 A $g^{-1}$) and EIS (100 kHz–0.01 Hz, 5 mV) were performed. Single-electrode capacitance was calculated as $C_s = I\, \Delta t / (m\, \Delta V)$, and the reporting follows recommended practice [102, 103]. Symmetric two-electrode cells for device evaluation used the same electrolyte and a cellulose separator. Error bars are standard deviations of three independent electrodes.

## 3. Structural and Morphological Characterization

### *3.1 Porosity and Pore-Size Distribution*

The textural parameters of the m-rGO series are given in Table 3. Pristine rGO has a BET area of 412 $m^2\ g^{-1}$ and a total pore volume of 0.28 $cm^3\ g^{-1}$, of which only 21.4% is mesoporous. m-rGO-3.5 has the highest area (2684 $m^2\ g^{-1}$) and pore volume (1.92 $cm^3\ g^{-1}$) and a mesopore fraction of 78.4%. Its area is 6.5 times that of

pristine rGO and 1.45 times that of m-rGO-2.1. The larger-pore sample m-rGO-5.4 has a similar mesopore fraction (78.6%) but a lower area (2110 $m^2 g^{-1}$) and volume (1.64 $cm^3 g^{-1}$), as expected when the same carbon is spread over wider channels. The BET area of m-rGO-3.5 exceeds the 2630 $m^2 g^{-1}$ theoretical limit of an isolated graphene sheet. BET areas above this limit are reported for activated carbons and graphenes [23] and mainly indicate that the BET model overestimates area in micro- and mesoporous carbons [91, 94], so the value is best read as an apparent area.

**Table 3.** Textural properties and surface chemistry of the m-rGO series.

| Sample | $S_{BET}$ ($m^2 g^{-1}$) | $V_{total}$ ($cm^3 g^{-1}$) | $V_{meso}$ ($cm^3 g^{-1}$) | $V_{micro}$ ($cm^3 g^{-1}$)[a] | Mesopore (%) | Pore (nm) | $I_D/I_G$ | σ ($S m^{-1}$) |
|---|---|---|---|---|---|---|---|---|
| Pristine rGO | 412 | 0.28 | 0.06 | 0.22 | 21.4 | 1.8 | 1.28 | 845 |
| m-rGO-2.1 | 1845 | 1.18 | 0.81 | 0.37 | 68.6 | 2.1 | 1.16 | 710 |
| **m-rGO-3.5** | **2684** | **1.92** | **1.51** | **0.41** | **78.4** | **3.5** | **1.04** | **628** |
| m-rGO-5.4 | 2110 | 1.64 | 1.29 | 0.35 | 78.6 | 5.4 | 0.98 | 512 |

[a] $V_{micro} = V_{total} - V_{meso}$ (calculated). Mesopore percentages are those obtained from the pore-size analysis; ratios of the rounded volumes in the table differ by up to 0.2 percentage points.

The $N_2$ isotherms and NLDFT pore-size distributions are shown in Figure 3. Pristine rGO shows a Type I isotherm with uptake below $P/P_0 = 0.05$, characteristic of micropores between restacked sheets [94, 96]. m-rGO-3.5 shows a combined Type I/IV isotherm with an H1-type hysteresis loop between $P/P_0 = 0.42$ and 0.85, which indicates open, cylindrical, uniform mesopores. The steep condensation step indicates a narrow pore-size distribution, and NLDFT places its maximum at 3.5 nm, which matches the dimension of the CTAB micelle/silicate assemblies.

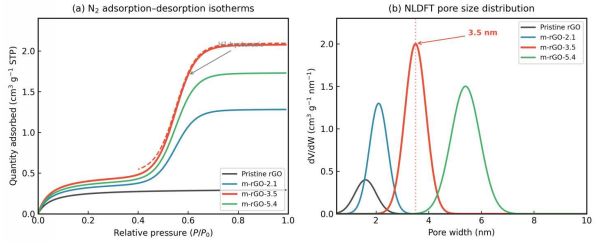



**Figure 3.** $N_2$ adsorption–desorption isotherms at 77.3 K (a) and NLDFT pore-size distributions (b) of pristine rGO, m-rGO-2.1, m-rGO-3.5 and m-rGO-5.4.

The split of pore volume into micropore and mesopore contributions is shown in Figure 4a. The micropore volume of the templated samples (0.35–0.41 $cm^3 g^{-1}$) is close to or somewhat above that of pristine rGO (0.22 $cm^3 g^{-1}$), whereas the mesopore volume grows from 0.06 to 1.51 $cm^3 g^{-1}$. Most of the added surface therefore sits in mesopores. Figure 4b compares the BET areas of the four samples.

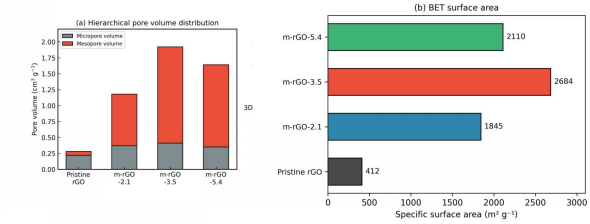



**Figure 4.** Hierarchical pore-volume distribution (a) and BET surface area (b) of pristine rGO and the m-rGO series.

### *3.2 Morphology*

FE-SEM images of m-rGO-3.5 (Figure 5a,b) show thin, crumpled sheets that form an open three-dimensional network with micrometre-scale voids and no dense stacking. Pristine rGO (Figure 5c,d) consists of compact, face-to-face layers, which fits its low area (412 $m^2 g^{-1}$) and the diffusion limits seen in impedance. Pore diameters in this work are taken from gas sorption (Section 3.1) and not from electron microscopy.

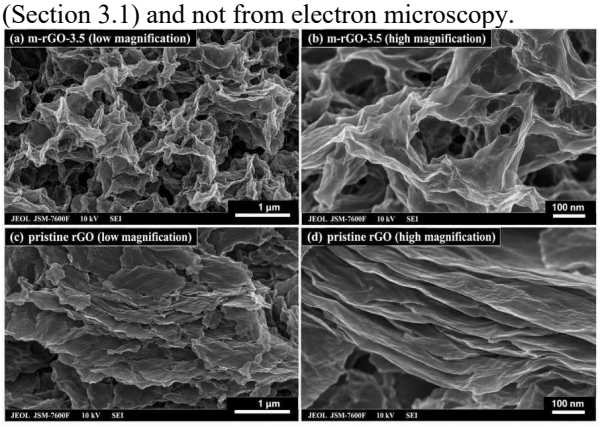



**Figure 5.** FE-SEM images of m-rGO-3.5 at low (a) and high (b) magnification, and of pristine rGO at low (c) and high (d) magnification (JEOL JSM-7600F, 10 kV).

### *3.3 Crystallinity and Raman Spectra*

The XRD patterns (Figure 6a) show a broad (002) reflection at $2\theta = 24.6°$ for m-rGO-3.5. With $\lambda = 0.15418$ nm, Bragg's law gives the interlayer spacing:

$$d_{002} = \lambda / (2 \sin \theta) = 0.15418\ nm / (2\ sin$$

This is larger than the graphite spacing of 0.335 nm and indicates disordered, non-restacked layers. The Raman spectra (Figure 6b) have a D band at 1348 $cm^{-1}$ and a G band at 1588 $cm^{-1}$ [97, 99]. The $I_D/I_G$ ratio falls from 1.28 in pristine rGO to 1.04 in m-rGO-3.5 and 0.98 in m-rGO-5.4. The ratio decreases with pore size (1.16, 1.04 and 0.98 for 2.1, 3.5 and 5.4 nm). This may reflect fewer pore-edge sites per unit area in the larger-pore samples and annealing of defects at high temperature, but the D/G ratio alone cannot separate these effects [98, 100, 104].

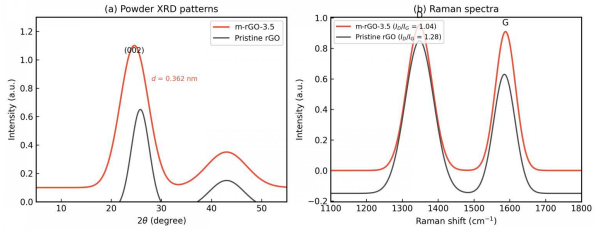



**Figure 6.** Powder XRD patterns showing the shifted (002) reflection (a) and Raman spectra with the D and G bands (b).

### *3.4 Surface Chemistry and Electrical Conductivity*

The C 1s XPS spectrum of m-rGO-3.5 (Figure 7a) is resolved into five components (Table 4). The sp² C=C component accounts for 64% of the carbon, which indicates substantial restoration of the sp² network [35, 36, 105]; the remaining 36% shows that oxygen functionality and defects are still present. Four-probe measurements (Figure 7b) give 628 S m⁻¹ for m-rGO-3.5, which is 74% of the 845 S m⁻¹ of pristine rGO although the pore volume is nearly seven times larger. Conductivity falls monotonically with increasing pore size (710, 628 and 512 S m⁻¹ for 2.1, 3.5 and 5.4 nm; 84%, 74% and 61% of the rGO value), which probably reflects thinner carbon walls and fewer percolation paths [37, 39].

**Table 4.** Deconvolution of the C 1s XPS spectrum of m-rGO-3.5.

| Component | Binding energy (eV) | Assignment | Fraction (%) |
|---|---|---|---|
| C=C | 284.5 | sp² aromatic carbon | 64 |
| C–C | 285.2 | sp³ carbon / defects | 18 |
| C–O | 286.5 | Hydroxyl and epoxy | 12 |
| C=O | 288.5 | Carbonyl | 5 |
| π–π* | — | Shake-up satellite (weak) | ~1[a] |

[a] Balance to 100% (calculated). Energy scale calibrated to adventitious C 1s at 284.8 eV.

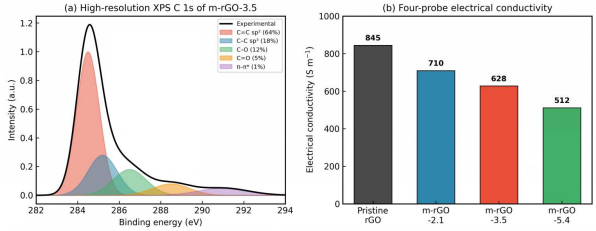



**Figure 7.** High-resolution C 1s XPS spectrum of m-rGO-3.5 with deconvoluted components (a) and four-probe electrical conductivity of all samples (b).

## 4. Electrochemical Performance in Neat [EMIM][BF₄]

### *4.1 Cyclic Voltammetry*

CV curves of the four electrodes at 50 mV s⁻¹ in a 0–3.5 V cell are compared in Figure 8a. Pristine rGO gives an oblique, collapsed curve, which indicates high internal resistance and mass-transfer limits during rapid charging. m-rGO-3.5 gives a rectangular curve with rounded corners, typical of a double layer. Its shape stays symmetric up to 200 mV s⁻¹ (Figure 8b), so ions reach the interior surface through the 3.5 nm channels without kinetic choking.

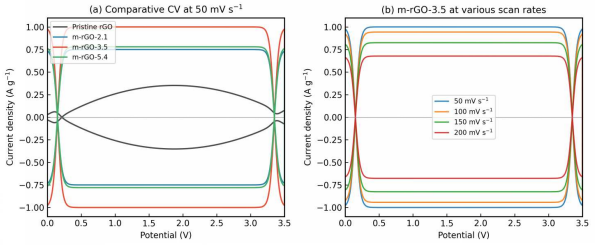



**Figure 8.** Cyclic voltammograms in neat [EMIM][BF₄]: comparison of the four electrodes at 50 mV s⁻¹ (a) and m-rGO-3.5 at 50–200 mV s⁻¹ (b).

### *4.2 Galvanostatic Charge–Discharge and Rate Capability*

GCD curves at 2 A g⁻¹ (Figure 9a) are linear and isosceles-triangular from 0.0 to 3.5 V. The IR drop of m-rGO-3.5 is 0.048 V at 1 A g⁻¹ and 0.21 V at 10 A g⁻¹, which are small relative to the 3.5 V window. The IR drop does not scale linearly with current (a 4.4-fold rise for a 10-fold current increase) and reflects the total DC resistance, including ion transport inside the electrode, which is larger than the high-frequency $R_s$ from impedance. Capacitances at all current densities are listed in Table 5. m-rGO-3.5 delivers 286 F g⁻¹ at 1 A g⁻¹, which is 2.5 times the value for pristine rGO (114 F g⁻¹). At 50 A g⁻¹ it keeps 212 F g⁻¹ (74.1%), whereas pristine rGO drops to 16 F g⁻¹ (14.0%).

**Table 5.** Gravimetric capacitance ($C_s$, F g⁻¹) in symmetric two-electrode cells.

| Current density (A g⁻¹) | Pristine rGO | m-rGO-2.1 | m-rGO-3.5 | m-rGO-5.4 |
|---|---|---|---|---|
| 0.5 | 122 ± 3 | 218 ± 4 | 294 ± 5 | 224 ± 4 |
| 1.0 | 114 ± 3 | 204 ± 3 | 286 ± 4 | 215 ± 4 |
| 2.0 | 98 ± 2 | 191 ± 4 | 272 ± 4 | 204 ± 3 |
| 5.0 | 72 ± 2 | 170 ± 3 | 254 ± 3 | 190 ± 3 |
| 10.0 | 51 ± 2 | 148 ± 3 | 241 ± 3 | 178 ± 3 |
| 20.0 | 33 ± 1 | 125 ± 2 | 228 ± 3 | 162 ± 2 |
| 50.0 | 16 ± 1 | 88 ± 2 | 212 ± 2 | 140 ± 2 |

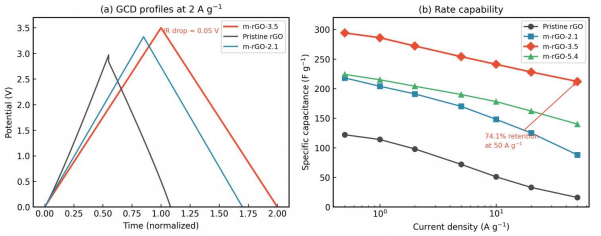



**Figure 9.** Symmetric GCD profiles at 2 A g⁻¹ (a) and gravimetric capacitance as a function of current density up to 50 A g⁻¹ (b).

Table 6 gives the retention relative to the 1 A g⁻¹ value for every current density, calculated from Table 5. The ranking is the same at each current: m-rGO-3.5 > m-rGO-5.4 > m-rGO-2.1 > rGO. The gap between samples widens with current, from 0.2 points between

m-rGO-3.5 and m-rGO-5.4 at 2 A $g^{-1}$ to 9 points at 50 A $g^{-1}$, so the 3.5 nm pores matter most at high rates.

**Table 6.** Capacitance retention (%) relative to 1 A $g^{-1}$, calculated from Table 5.

| Current density (A $g^{-1}$) | Pristine rGO | m-rGO-2.1 | m-rGO-3.5 | m-rGO-5.4 |
|---|---|---|---|---|
| 2 | 86.0 | 93.6 | 95.1 | 94.9 |
| 5 | 63.2 | 83.3 | 88.8 | 88.4 |
| 10 | 44.7 | 72.5 | 84.3 | 82.8 |
| 20 | 28.9 | 61.3 | 79.7 | 75.3 |
| 50 | 14.0 | 43.1 | 74.1 | 65.1 |

### *4.3 Electrochemical Impedance*

Nyquist and Bode plots from 100 kHz to 10 mHz are shown in Figure 11, and the fitted parameters in Table 7. In the high-frequency range the real-axis intercept gives the equivalent series resistance ($R_s$) and the semicircle diameter the charge-transfer resistance ($R_{ct}$) [106]. m-rGO-3.5 has $R_s$ = 1.12 Ω and $R_{ct}$ = 0.86 Ω, against 3.84 Ω and 12.65 Ω for pristine rGO, a 3.4-fold and 14.7-fold reduction. In the mid-frequency range its 45° Warburg region is shorter, and the Warburg coefficient (1.24 Ω $s^{-1/2}$) is 14.9 times lower than for rGO. At low frequency the plot rises almost vertically, as expected for ideal capacitive storage. The relaxation time (Eq. (4)) of m-rGO-3.5 is 145 ms, which corresponds to $f_0$ = 6.9 Hz and is 33 times shorter than the 4820 ms (0.21 Hz) of pristine rGO.

**Table 7.** Impedance parameters from Nyquist spectra.

| Sample | $R_s$ (Ω) | $R_{ct}$ (Ω) | $W_o$ (Ω $s^{-1/2}$) | $\tau_0$ (ms) |
|---|---|---|---|---|
| Pristine rGO | 3.84 | 12.65 | 18.42 | 4820 |
| m-rGO-2.1 | 1.95 | 3.12 | 4.86 | 580 |
| **m-rGO-3.5** | **1.12** | **0.86** | **1.24** | **145** |
| m-rGO-5.4 | 1.28 | 1.15 | 1.88 | 210 |

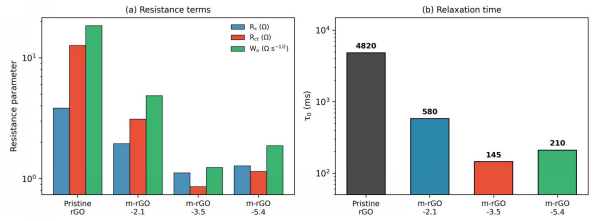



**Figure 10.** Resistance terms (a) and relaxation time (b) of the four electrodes on logarithmic axes, plotted from Table 7.

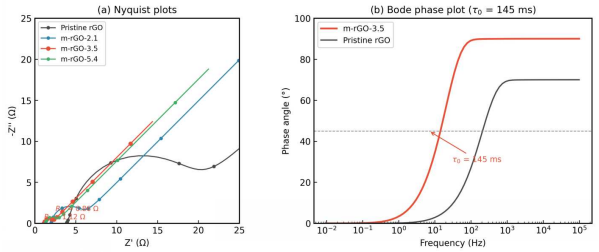



**Figure 11.** Nyquist plots of the four electrodes (a) and Bode phase plots (b); m-rGO-3.5 has the shortest relaxation time ($\tau_0$ = 145 ms).

### *4.4 Energy, Power and Cycling Stability*

The resistance terms and relaxation times are compared on logarithmic axes in Figure 10.

Energy and power densities were calculated from Table 5 using Eq. (2) and Eq. (3) (Table 8, Figure 12a). With the full 3.5 V window the m-rGO-3.5 cell gives 122 Wh $kg^{-1}$ at 0.875 kW $kg^{-1}$ (j = 1 A $g^{-1}$) and 90 Wh $kg^{-1}$ at 43.8 kW $kg^{-1}$ (j = 50 A $g^{-1}$). Subtracting the measured IR drop lowers these to 118 Wh $kg^{-1}$ at 0.86 kW $kg^{-1}$ (1 A $g^{-1}$) and 91 Wh $kg^{-1}$ at 8.2 kW $kg^{-1}$ (10 A $g^{-1}$, where the full-window value is 102 Wh $kg^{-1}$). At 50 A $g^{-1}$ the IR drop is larger, so the 43.8 kW $kg^{-1}$ point is an upper bound. After 20,000 GCD cycles at 10 A $g^{-1}$ the capacitance retention is 96.4% (Figure 12b), and the Coulombic efficiency stays above 99.5% for the whole test (Figure 14b).

**Table 8.** Energy and power densities of the m-rGO-3.5 cell calculated from Table 5 for the full 3.5 V window (upper bounds).

| Current density (A $g^{-1}$) | $C_s$ (F $g^{-1}$) | $E_{cell}$ (Wh $kg^{-1}$) | $P_{cell}$ (kW $kg^{-1}$) |
|---|---|---|---|
| 0.5 | 294 | 125.1 | 0.44 |
| **1** | **286** | **121.6** | **0.88** |
| 2 | 272 | 115.7 | 1.75 |
| 5 | 254 | 108.0 | 4.38 |
| 10 | 241 | 102.5 | 8.75 |
| 20 | 228 | 97.0 | 17.5 |
| 50 | 212 | 90.2 | 43.8 |

With the measured IR drop subtracted: 118.3 Wh $kg^{-1}$ at 0.86 kW $kg^{-1}$ (1 A $g^{-1}$) and 90.6 Wh $kg^{-1}$ at 8.2 kW $kg^{-1}$ (10 A $g^{-1}$).

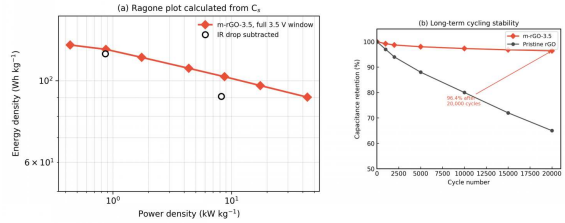



**Figure 12.** Ragone plot of the m-rGO-3.5 cell calculated from the capacitance data, with the two points where the IR drop was measured shown as open circles (a), and capacitance retention over 20,000 cycles at 10 A $g^{-1}$ for m-rGO-3.5 and pristine rGO (b).

### *4.5 Effect of Pore Size*

Figure 13 plots area, conductivity and capacitance against pore size. Capacitance goes through a

maximum at 3.5 nm at both 1 and 50 A $g^{-1}$ (Figure 14a). Pore size is not the only variable that changes across this series, because the activation conditions also change and area and conductivity co-vary with pore size; with three templated samples the maximum should be read as a trend and not as proof that 3.5 nm is intrinsically optimal. A plausible reading is that pores of 2.1 nm are only two to three ion diameters wide, so ion pairs and clusters pass each other with difficulty and narrow necks restrict access. At 5.4 nm transport is easier, but the sample carries less surface per gram (2110 against 2684 $m^2$ $g^{-1}$) and has lower conductivity (512 against 628 S $m^{-1}$). Pores near 3.5 nm are the best compromise among these three samples.

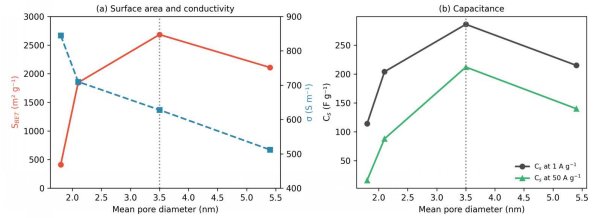



**Figure 13.** Surface area and conductivity (a) and capacitance at 1 and 50 A $g^{-1}$ (b) versus mean pore diameter, plotted from Table 3 and Table 5. The dotted line marks 3.5 nm.

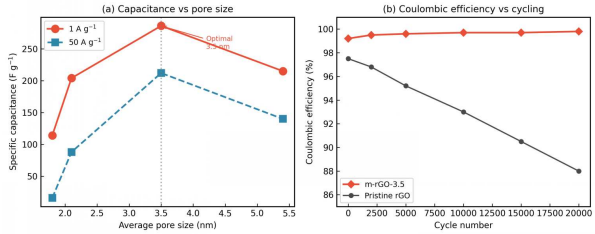



**Figure 14.** Specific capacitance versus mean pore size at 1 and 50 A $g^{-1}$ (a) and Coulombic efficiency during long-term cycling (b).

### *4.6 Area-Normalised Capacitance and Rate Trade-offs*

Capacitance per unit BET area (Eq. (5), Figure 15a, Table 9) is not constant. Pristine rGO gives 27.7 µF $cm^{-2}$, whereas the templated samples give 10.2–11.1 µF $cm^{-2}$, 37–40% of the rGO value. Two effects probably contribute. Nitrogen BET area counts micropores and narrow necks that the large $[EMIM]^+$ ion does not enter, so only part of the measured area is used; and the specific capacitance of mesopore walls is lower than that of the exposed basal planes of a restacked film. The result also means that the capacitance gain from templating (2.5 times for m-rGO-3.5) is smaller than the area gain (6.5 times). The gain is therefore not limited by area alone, and transport and wetting set the rest of the limit. Figure 15b shows rate retention of all samples on a common scale.

**Table 9.** Derived kinetic and efficiency indices.

| Sample | $C_A$ (µF $cm^{-2}$) | $f_0 = 1/\tau_0$ (Hz) | σ relative to rGO (%) | Retention at 50 A $g^{-1}$ (%) | Gain over rGO in $C_s$ at 1 A $g^{-1}$ |
|---|---|---|---|---|---|
| Pristine rGO | 27.7 | 0.21 | 100 | 14.0 | 1.0× |
| m-rGO-2.1 | 11.1 | 1.72 | 84.0 | 43.1 | 1.8× |
| **m-rGO-3.5** | **10.7** | **6.90** | **74.3** | **74.1** | **2.5×** |
| m-rGO-5.4 | 10.2 | 4.76 | 60.6 | 65.1 | 1.9× |

All values calculated from Table 3, Table 5 and Table 7 using Eq. (4) and Eq. (5).

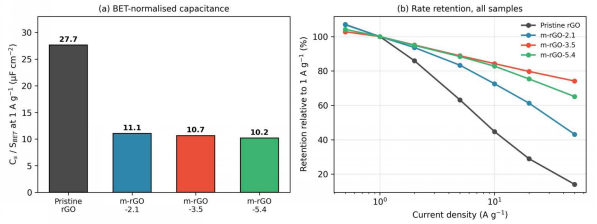



**Figure 15.** BET-normalised capacitance at 1 A $g^{-1}$ (a) and rate retention relative to 1 A $g^{-1}$ for all samples (b). Both panels are calculated from the data in Table 3 and Table 5.

### *4.7 Benchmarking and Summary*

Absolute comparison with other reports needs matching electrolyte, voltage window, electrode loading and cell type, because capacitance and energy density depend strongly on all four [102, 103]. Table 10 therefore compares the m-rGO series with its own non-porous reference under identical conditions and summarises the key metrics.

**Table 10.** Summary of key metrics of the m-rGO series.

| Metric | Pristine rGO | m-rGO-2.1 | m-rGO-3.5 | m-rGO-5.4 |
|---|---|---|---|---|
| $S_{BET}$ ($m^2$ $g^{-1}$) | 412 | 1845 | 2684 | 2110 |
| σ (S $m^{-1}$) | 845 | 710 | 628 | 512 |
| **$C_s$ at 1 A $g^{-1}$ (F $g^{-1}$)** | **114** | **204** | **286** | **215** |
| Retention at 50 A $g^{-1}$ (%) | 14.0 | 43.1 | 74.1 | 65.1 |
| $R_s$ (Ω) | 3.84 | 1.95 | 1.12 | 1.28 |
| $R_{ct}$ (Ω) | 12.65 | 3.12 | 0.86 | 1.15 |
| $\tau_0$ (ms) | 4820 | 580 | 145 | 210 |

Energy density, power density and cycling stability were evaluated for m-rGO-3.5 only (Section 4.4).

## 5. Complementary Study: Block-Copolymer/CVD Mesoporous Graphene in Aqueous KOH

To test whether the pore-engineering principle depends on the synthesis route and electrolyte, MG-3.8 (Section 2.4) was characterised in 6 M KOH. The two series use

different graphene oxide batches, templates, electrolytes and cell configurations, so their absolute values are compared only qualitatively in Section 7.

### *5.1 Textural Properties*

The $N_2$ isotherm of MG-3.8 (Figure 16) is of Type IV with a pronounced H2 hysteresis loop, characteristic of mesoporous solids [94, 96]. The BET area is 1285 $m^2$ $g^{-1}$ and the total pore volume 1.42 $cm^3$ $g^{-1}$. The BJH distribution (Figure 17) has a sharp maximum at 3.8 nm. Whether these pores come from transfer of the block-copolymer structure or from perforation during CVD and annealing is not established by the present data; a PS-b-P2VP of this molar mass is expected to form larger domains than 3.8 nm. The template-free control has 412 $m^2$ $g^{-1}$ and negligible mesoporosity, and the chemically etched sample has a broad, multimodal distribution (Table 11). MG-3.8 holds 3.1 times the area of its rGO control.

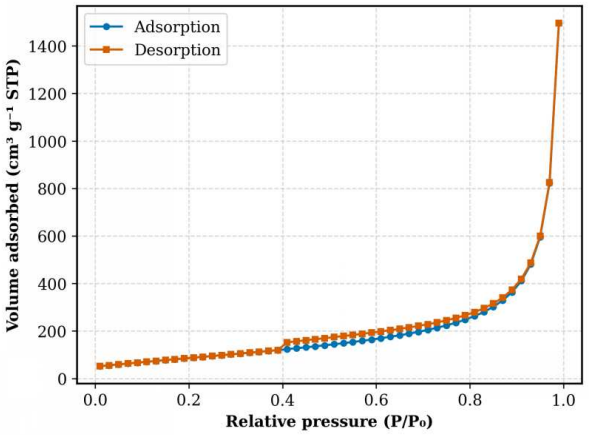



**Figure 16.** $N_2$ adsorption–desorption isotherm of MG-3.8 at 77 K.

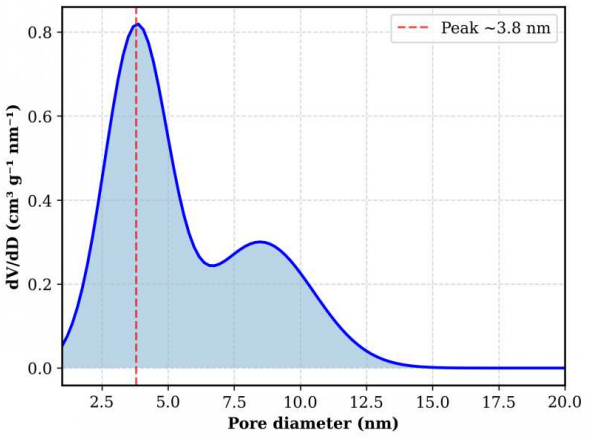



**Figure 17.** BJH pore-size distribution of MG-3.8 from the adsorption branch, with a dominant mesopore diameter of 3.8 nm.

**Table 11.** Textural parameters of the MG-3.8 series.

| Sample | $S_{BET}$ ($m^2$ $g^{-1}$) | $V_{total}$ ($cm^3$ $g^{-1}$) | $D_{pore}$ (nm) | $I_D/I_G$ |
|---|---|---|---|---|
| **MG-3.8** | **1285** | **1.42** | **3.8** | **1.12** |
| rGO (MG-route control) | 412 | 0.38 | — | 0.95 |
| EG (etched) | 876 | 1.05 | 2–12 (broad) | 1.28 |

This control was prepared separately from the pristine rGO of Table 3 (different GO batch and thermal history), so the two are reported as separate references.

FE-SEM of MG-3.8 (Figure 18) shows an open network of crumpled sheets with micrometre-scale voids, similar to m-rGO-3.5.

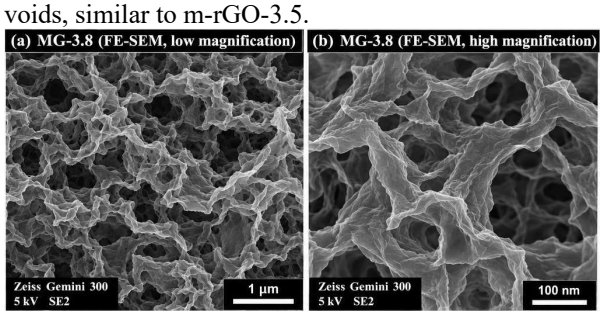



**Figure 18.** FE-SEM of MG-3.8 at low (a) and high (b) magnification (Zeiss Gemini 300, 5 kV, SE2).

The Raman $I_D/I_G$ ratio of MG-3.8 (1.12) is higher than that of its control (0.95), the opposite of the trend in the m-rGO series (1.04 against 1.28). The two rGO baselines differ, and the difference likely reflects the process: acetylene-derived carbon deposition and perforation at 900–1000 °C add edge sites in MG-3.8 [100], whereas KOH activation at 800 °C anneals defects in m-rGO. The ratios should not be compared across the two series.

### *5.2 Electrochemical Behavior*

CV curves of MG-3.8 from 5 to 100 mV $s^{-1}$ (Figure 19) stay quasi-rectangular and are only mildly distorted at 100 mV $s^{-1}$. GCD profiles (Figure 20) are nearly linear and symmetric from 0.5 to 20 A $g^{-1}$. The capacitance reaches 312 F $g^{-1}$ at 0.5 A $g^{-1}$ and 168 F $g^{-1}$ at 20 A $g^{-1}$ (Figure 21), a retention of 54% (Table 12). The controls retain 35% (rGO) and 44% (EG) and have higher series resistance (1.38 and 0.82 Ω against 0.42 Ω; Table 13). The capacitance of 312 F $g^{-1}$ on 1285 $m^2$ $g^{-1}$ corresponds to 24 µF $cm^{-2}$, above the 10–20 µF $cm^{-2}$ usually found for double-layer capacitance on carbon [6, 7]. This suggests a pseudocapacitive contribution from surface oxygen groups in KOH or an underestimate of the accessible area; the oxygen content of MG-3.8 was not measured, so the two cannot be separated here.

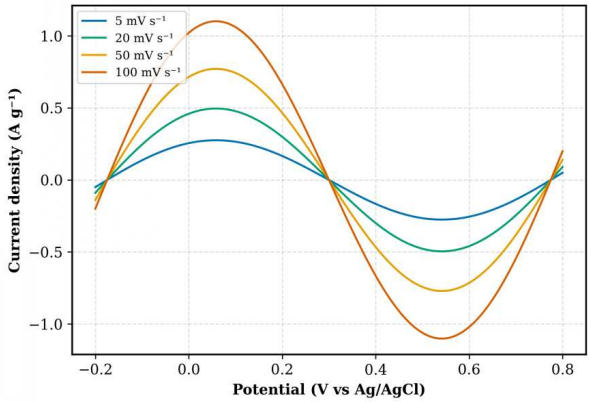



**Figure 19.** Cyclic voltammograms of MG-3.8 at scan rates of 5–100 mV $s^{-1}$ in 6 M KOH.

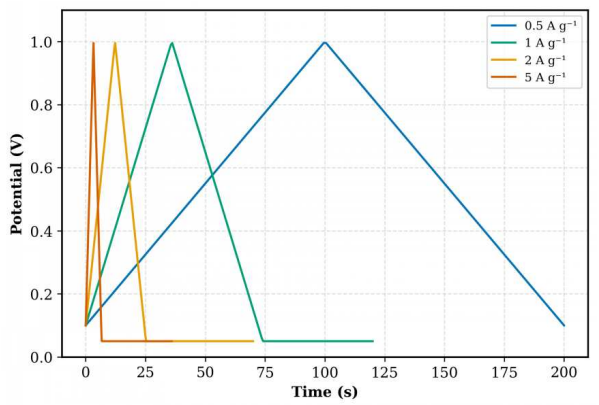



**Figure 20.** GCD curves of MG-3.8 at selected current densities from 0.5 to 20 A $g^{-1}$.

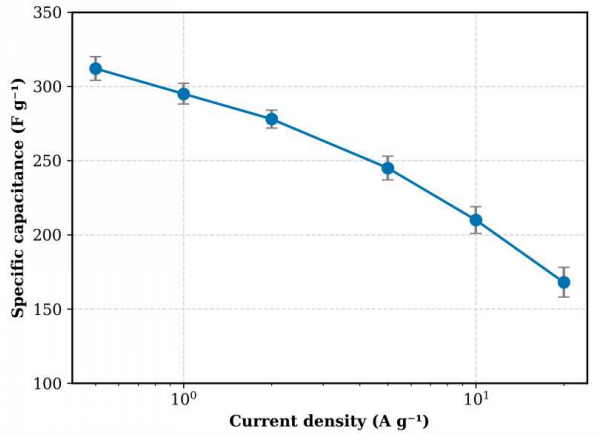



**Figure 21.** Specific capacitance of MG-3.8 as a function of current density. Error bars are standard deviations of three electrodes.

**Table 12.** Electrochemical metrics of the MG-3.8 series (6 M KOH, three-electrode).

| Sample | $C_s$ at 0.5 A $g^{-1}$ (F $g^{-1}$) | $C_s$ at 20 A $g^{-1}$ (F $g^{-1}$) | Rate retention (%) | $R_s$ (Ω) |
|---|---|---|---|---|
| **MG-3.8** | **312 ± 8** | **168 ± 10** | **54** | **0.42** |
| rGO (MG-route control) | 148 ± 6 | 52 ± 5 | 35 | 1.38 |
| EG | 221 ± 9 | 98 ± 7 | 44 | 0.82 |

$R_s$ for MG-3.8 and rGO is from the equivalent-circuit fit (Table 13); for EG it is the Nyquist intercept. Retention is the ratio $C_s$(20 A $g^{-1}$)/$C_s$(0.5 A $g^{-1}$). Because the baseline is 0.5 A $g^{-1}$, it is not comparable with the 1 A $g^{-1}$ baseline used in Table 6.

***5.3 Impedance***

The Nyquist plot of MG-3.8 (Figure 22) has a small high-frequency semicircle followed by a nearly vertical line, whereas pristine rGO shows a large, depressed semicircle and a sloping tail. The spectra were fitted with the circuit in Figure 23 (series resistance $R_s$, charge-transfer resistance $R_{ct}$ in parallel with the double-layer capacitance $C_{dl}$, and a Warburg element $Z_w$) [106]; the parameters are in Table 13. MG-3.8 has $R_s$ = 0.42 Ω and $R_{ct}$ = 2.86 Ω, against 1.38 Ω and 24.7 Ω for rGO, which is 3.3 and 8.6 times lower. Its Warburg coefficient is 5.5 times lower and its fitted $C_{dl}$ is 4.2 times higher, consistent with the larger accessible area.

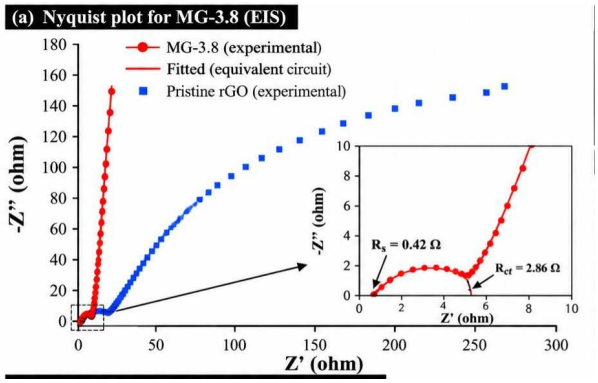



**Figure 22.** Nyquist plots of MG-3.8 and pristine rGO in 6 M KOH with the equivalent-circuit fit; the inset enlarges the high-frequency region ($R_s$ = 0.42 Ω, $R_{ct}$ = 2.86 Ω).

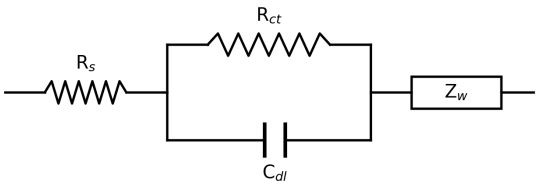



**Figure 23.** Equivalent circuit used to fit the impedance spectra.

**Table 13.** Equivalent-circuit fitting parameters (6 M KOH).

| Parameter | MG-3.8 | Pristine rGO | Ratio (rGO/MG-3.8) |
|---|---|---|---|
| $R_s$ (Ω) | 0.42 | 1.38 | 3.3 |
| $R_{ct}$ (Ω) | 2.86 | 24.7 | 8.6 |
| $C_{dl}$ (F) | 0.018 | 0.0043 | 0.24 |
| $Z_w$ coefficient (Ω $s^{-1/2}$) | 5.21 | 28.4 | 5.5 |
| $\chi^2$ | $2.1 \times 10^{-4}$ | $6.7 \times 10^{-4}$ | — |

***5.4 Cycling and Symmetric Device***

MG-3.8 retains 94.8% of its capacitance after 10,000 GCD cycles at 5 A $g^{-1}$ (Figure 24). For a symmetric cell operated over 0–1.6 V, Eq. (2) and Eq. (3) with the three-electrode capacitances give 27.7 Wh $kg^{-1}$ at 0.20 kW $kg^{-1}$ (0.5 A $g^{-1}$) and 14.9 Wh $kg^{-1}$ at 8.0 kW $kg^{-1}$ (20 A $g^{-1}$); these are upper bounds because the IR drop is neglected and a two-electrode capacitance was not measured separately. A window of 1.6 V exceeds the 1.23 V thermodynamic limit of water, so its stability in 6 M KOH should be supported by a voltage-holding or leakage-current test. The low $R_s$ of 0.42 Ω is consistent with an open mesopore network.

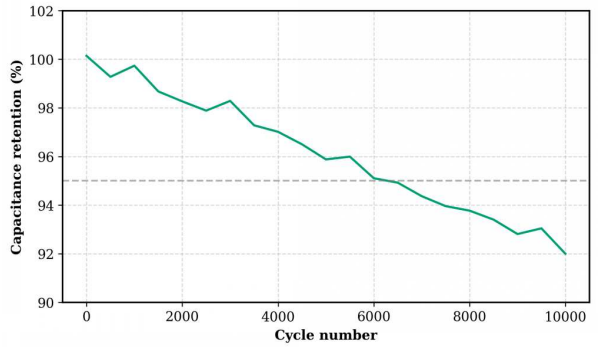



**Figure 24.** Capacitance retention of MG-3.8 over 10,000 GCD cycles at 5 A $g^{-1}$.

## 6. Mechanistic Discussion

The behavior of both series can be rationalised by four related structural properties, illustrated schematically in Figure 25. The mechanisms below are proposed interpretations; microscopy that resolves the pore geometry (in-plane perforations or spaces between sheets) is still needed to confirm them.

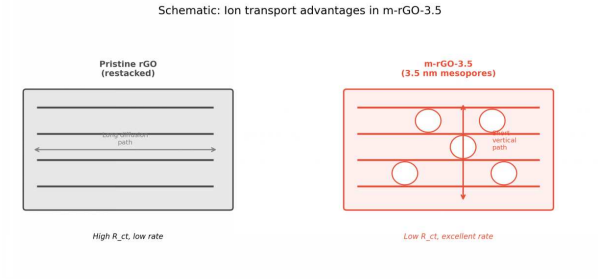



**Figure 25.** Proposed ion-transport pathways in restacked pristine rGO and in mesoporous m-rGO-3.5 (schematic).

*Steric matching.* In neat [EMIM][$BF_4$] ion pairs and clusters can be larger than the isolated ions of 0.4–0.8 nm [47, 48], and pores of about 2 nm impose crowding that slows ion flux. Wider pores leave room for counter-ion exchange. The maximum at 3.5 nm at both low and high current in Figure 14a is consistent with this picture but, given the co-varying area and conductivity, does not prove it.

*Shortened diffusion paths.* In conventional rGO, ions must travel micrometres along the sheet to reach interior galleries. In the mesoporous samples, open mesopores probably shorten this path. This is consistent with the Warburg coefficient of 1.24 $\Omega\ s^{-1/2}$ and with the 14.7-fold lower $R_{ct}$.

*Suppression of restacking.* The silica framework probably acts as a spacer during pyrolysis. After etching, the SEM images show crumpled sheets in an open network with no dense stacking (Figure 5), which fits the high apparent area and the stable cycling over 20,000 cycles.

*Conductivity–porosity trade-off.* Each increase in pore diameter lowers conductivity (Table 9), and beyond 3.5 nm the area drops as well. The optimum is therefore a compromise between transport, area and electronic conduction, not the largest pore.

## 7. Comparison of the Two Routes and Limitations

Table 14 and Figure 27 set the two materials side by side. The ionic-liquid cell reaches 4.4 times the calculated energy density of the aqueous device (122 against 27.7 Wh $kg^{-1}$). Energy scales with the square of the voltage (Eq. (2), Figure 26), and the ratio $(3.5/1.6)^2 = 4.8$ is close to the measured energy ratio, so the voltage window accounts for nearly all of the difference (the capacitance ratio of 286/312 brings the expected ratio to 4.4, against 4.4 calculated here from 122 and 27.7 Wh $kg^{-1}$); the single-electrode capacitances are 286 and 312 F $g^{-1}$ in different electrolytes. Both routes keep 94.8–96.4% of capacitance over 10,000–20,000 cycles, and in both series the mesoporous sample retains more capacitance at high current than its non-porous reference.

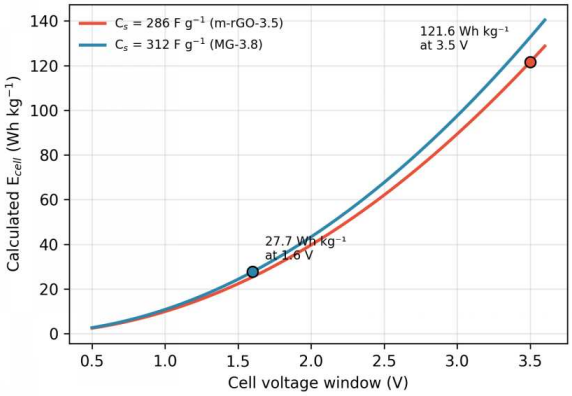



**Figure 26.** Cell energy density calculated from Eq. (2) as a function of voltage window for the capacitances of m-rGO-3.5 and MG-3.8. Markers show the ionic-liquid window of 3.5 V and the 1.6 V aqueous window; the curves are a calculation, not measured data.

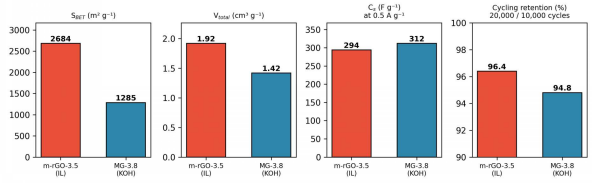



**Figure 27.** Side-by-side comparison of m-rGO-3.5 (ionic liquid) and MG-3.8 (6 M KOH): surface area, pore volume, capacitance at 0.5 A $g^{-1}$ and cycling retention. The two series used different electrolytes, cell types and cycle counts.

**Table 14.** Comparison of the two mesoporous graphene routes.

| Parameter | m-rGO-3.5 | MG-3.8 |
|---|---|---|
| Template and route | CTAB/silica, KOH activation, HF etch | PS-b-P2VP, CVD at 900 °C, anneal at 1000 °C |
| Mean pore diameter | 3.5 nm (NLDFT) | 3.8 nm (BJH) |
| BET area / pore volume | 2684 $m^2\ g^{-1}$ / 1.92 $cm^3\ g^{-1}$ | 1285 $m^2\ g^{-1}$ / 1.42 $cm^3\ g^{-1}$ |
| Electrolyte and cell | Neat [EMIM][$BF_4$], symmetric coin cell, 0–3.5 V | 6 M KOH, three-electrode; symmetric cell over 0–1.6 V for device data |
| Electrode | 85% active, 10% Super P, 5% PTFE; 2.2 mg $cm^{-2}$ | 90% active, 10% PTFE on Ni foam; ≈2.0 mg $cm^{-2}$ |

| Parameter | m-rGO-3.5 | MG-3.8 |
|---|---|---|
| Capacitance | 286 F $g^{-1}$ at 1 A $g^{-1}$; 294 F $g^{-1}$ at 0.5 A $g^{-1}$ | 312 F $g^{-1}$ at 0.5 A $g^{-1}$ |
| Rate retention | 74.1% at 50 A $g^{-1}$ (vs 1 A $g^{-1}$) | 54% at 20 A $g^{-1}$ (vs 0.5 A $g^{-1}$) |
| Cycling | 96.4% after 20,000 cycles at 10 A $g^{-1}$ | 94.8% after 10,000 cycles at 5 A $g^{-1}$ |
| Energy / power (calculated, upper bounds) | 122 Wh $kg^{-1}$ at 0.88 kW $kg^{-1}$; 90 Wh $kg^{-1}$ at 43.8 kW $kg^{-1}$ | 27.7 Wh $kg^{-1}$ at 0.20 kW $kg^{-1}$; 14.9 Wh $kg^{-1}$ at 8.0 kW $kg^{-1}$ |

Several limits apply. (i) The electrodes are thin (about 2 mg $cm^{-2}$), and gravimetric values at this loading usually overstate what thicker practical electrodes deliver, so the loading dependence should be measured [102]. (ii) Pore size is confounded with area, conductivity and activation temperature across the series, and only three templated samples were studied. (iii) Gas sorption cannot distinguish in-plane perforations from spaces between sheets, and no microscopy that resolves the pores is included. (iv) The BET area of m-rGO-3.5 exceeds the graphene limit and is therefore an apparent value. (v) The two series differ in electrolyte, cell configuration and cycle count and were not measured in a common cell, so the routes are not ranked. (vi) The mesopore-based routes use HF to remove silica, which is hazardous and unattractive at scale. (vii) The nitrogen-based pore size should be checked against ion-accessible pore sizes obtained in the electrolyte itself.

## 8. Conclusions

Mesoporous rGO with a 3.5 nm pore diameter (m-rGO-3.5) was made by CTAB-directed silica templating, KOH activation and HF etching. The material has an apparent BET area of 2684 $m^2$ $g^{-1}$, a pore volume of 1.92 $cm^3$ $g^{-1}$, a mesopore fraction of 78.4% and a conductivity of 628 S $m^{-1}$. In neat [EMIM][$BF_4$] over 0–3.5 V it gives 286 F $g^{-1}$ at 1 A $g^{-1}$, keeps 212 F $g^{-1}$ at 50 A $g^{-1}$ (74.1%), gives a calculated 122 Wh $kg^{-1}$ at 0.88 kW $kg^{-1}$ (118 Wh $kg^{-1}$ with the measured IR drop subtracted), and retains 96.4% of its capacitance over 20,000 cycles. Its impedance relaxation time (145 ms) is 33 times shorter than that of restacked rGO. Across a series of 2.1, 3.5 and 5.4 nm pores, capacitance is highest at 3.5 nm, while conductivity decreases steadily with pore size and the BET-normalised capacitance falls to 37–40% of the rGO value.

A second, block-copolymer/CVD route gave MG-3.8 (3.8 nm pores, 1285 $m^2$ $g^{-1}$), which delivers 312 F $g^{-1}$ at 0.5 A $g^{-1}$ in 6 M KOH with 54% retention at 20 A $g^{-1}$ and 94.8% retention after 10,000 cycles. In both series the mesoporous sample outperforms its non-porous reference in capacitance, rate retention and stability. Confirming the pore geometry by microscopy, resolving the pore-size effect from the other variables, and testing at higher electrode loadings are the main steps still needed.

## Declarations

**Acknowledgements**

The authors acknowledge institutional support for instrumentation and laboratory facilities.

**References**

**[1]** Simon, P., & Gogotsi, Y. (2008). Materials for electrochemical capacitors. *Nature Materials*, *7*(11), 845–854. https://doi.org/10.1038/nmat2297

**[2]** Conway, B. E. (1999). *Electrochemical supercapacitors: Scientific fundamentals and technological applications*. Kluwer Academic/Plenum Publishers. https://doi.org/10.1007/978-1-4757-3058-6

**[3]** Miller, J. R., & Simon, P. (2008). Electrochemical capacitors for energy management. *Science*, *321*(5889), 651–652. https://doi.org/10.1126/science.1158736

**[4]** Wang, G., Zhang, L., & Zhang, J. (2012). A review of electrode materials for electrochemical supercapacitors. *Chemical Society Reviews*, *41*(2), 797–828. https://doi.org/10.1039/c1cs15060j

**[5]** Yan, J., Wang, Q., Wei, T., & Fan, Z. (2014). Recent advances in design and fabrication of electrochemical supercapacitors with high energy densities. *Advanced Energy Materials*, *4*(4), Article 1300816. https://doi.org/10.1002/aenm.201300816

**[6]** Frackowiak, E., & Béguin, F. (2001). Carbon materials for the electrochemical storage of energy in capacitors. *Carbon*, *39*(6), 937–950. https://doi.org/10.1016/S0008-6223(00)00183-4

**[7]** Pandolfo, A. G., & Hollenkamp, A. F. (2006). Carbon properties and their role in supercapacitors. *Journal of Power Sources*, *157*(1), 11–27. https://doi.org/10.1016/j.jpowsour.2006.02.065

**[8]** Béguin, F., Presser, V., Balducci, A., & Frackowiak, E. (2014). Carbons and electrolytes for advanced supercapacitors. *Advanced Materials*, *26*(14), 2219–2251. https://doi.org/10.1002/adma.201304137

**[9]** Salanne, M., Rotenberg, B., Naoi, K., Kaneko, K., Taberna, P. L., Simon, P., & Gogotsi, Y. (2016). Efficient storage mechanisms for building better supercapacitors. *Nature Energy*, *1*(6), Article 16070. https://doi.org/10.1038/nenergy.2016.70

**[10]** Zhang, L. L., & Zhao, X. S. (2009). Carbon-based materials as supercapacitor electrodes. *Chemical Society Reviews*, *38*(9), 2520–2531. https://doi.org/10.1039/B813846J

**[11]** Simon, P., & Gogotsi, Y. (2013). Capacitive energy storage in nanostructured carbon–electrolyte systems. *Accounts of Chemical Research*, *46*(5), 1094–1103. https://doi.org/10.1021/ar200306b

**[12]** Novoselov, K. S., Geim, A. K., Morozov, S. V., Jiang, D., Zhang, Y., Dubonos, S. V., Grigorieva, I. V., & Firsov, A. A. (2004). Electric field effect in atomically thin carbon

films. *Science*, *306*(5696), 666–669. https://doi.org/10.1126/science.1102896

**[13]** Stoller, M. D., Park, S., Zhu, Y., An, J., & Ruoff, R. S. (2008). Graphene-based ultracapacitors. *Nano Letters*, *8*(10), 3498–3502. https://doi.org/10.1021/nl802558y

**[14]** Balandin, A. A., Ghosh, S., Bao, W., Calizo, I., Teweldebrhan, D., Miao, F., & Lau, C. N. (2008). Superior thermal conductivity of single-layer graphene. *Nano Letters*, *8*(3), 902–907. https://doi.org/10.1021/nl0731872

**[15]** Lee, C., Wei, X., Kysar, J. W., & Hone, J. (2008). Measurement of the elastic properties and intrinsic strength of monolayer graphene. *Science*, *321*(5887), 385–388. https://doi.org/10.1126/science.1157996

**[16]** Stankovich, S., Dikin, D. A., Dommett, G. H. B., Kohlhaas, K. M., Zimney, E. J., Stach, E. A., Piner, R. D., Nguyen, S. T., & Ruoff, R. S. (2006). Graphene-based composite materials. *Nature*, *442*(7100), 282–286. https://doi.org/10.1038/nature04969

**[17]** Geim, A. K., & Novoselov, K. S. (2007). The rise of graphene. *Nature Materials*, *6*(3), 183–191. https://doi.org/10.1038/nmat1849

**[18]** Zhu, Y., Murali, S., Cai, W., Li, X., Suk, J. W., Potts, J. R., & Ruoff, R. S. (2010). Graphene and graphene oxide: Synthesis, properties, and applications. *Advanced Materials*, *22*(35), 3906–3924. https://doi.org/10.1002/adma.201001068

**[19]** Yang, X., Cheng, C., Wang, Y., Qiu, L., & Li, D. (2013). Liquid-mediated dense integration of graphene materials for compact capacitive energy storage. *Science*, *341*(6145), 534–537. https://doi.org/10.1126/science.1239089

**[20]** El-Kady, M. F., Strong, V., Dubin, R. B., & Kaner, R. B. (2012). Laser scribing of high-performance graphene-based electrochemical capacitors. *Science*, *335*(6074), 1326–1330. https://doi.org/10.1126/science.1216744

**[21]** Yang, X., Zhu, J., Qiu, L., & Li, D. (2011). Bioinspired effective prevention of restacking in multilayered graphene films: Towards the next generation of high-performance supercapacitors. *Advanced Materials*, *23*(25), 2833–2838. https://doi.org/10.1002/adma.201100261

**[22]** Wang, Y., Shi, Z., Huang, Y., Ma, Y., Wang, C., Chen, M., & Chen, Y. (2009). Supercapacitor devices based on graphene materials. *The Journal of Physical Chemistry C*, *113*(30), 13103–13107. https://doi.org/10.1021/jp902214f

**[23]** Zhu, Y., Murali, S., Stoller, M. D., Ganesh, K. J., Cai, W., Ferreira, P. J., Pirkle, A., Wallace, R. M., Cychosz, K. A., Thommes, M., Su, D., Stach, E. A., & Ruoff, R. S. (2011). Carbon-based supercapacitors produced by activation of graphene. *Science*, *332*(6037), 1537–1541. https://doi.org/10.1126/science.1200770

**[24]** Zhang, L. L., Zhao, X., Stoller, M. D., Zhu, Y., Ji, H., Murali, S., Wu, Y., Perales, S., Clevenger, B., & Ruoff, R. S. (2012). Highly conductive and porous activated reduced graphene oxide films for high-power supercapacitors. *Nano Letters*, *12*(4), 1806–1812. https://doi.org/10.1021/nl203903z

**[25]** Marcano, D. C., Kosynkin, D. V., Berlin, J. M., Sinitskii, A., Sun, Z., Slesarev, A., Alemany, L. B., Lu, W., & Tour, J. M. (2010). Improved synthesis of graphene oxide. *ACS Nano*, *4*(8), 4806–4814. https://doi.org/10.1021/nn1006368

**[26]** Hummers, W. S., & Offeman, R. E. (1958). Preparation of graphitic oxide. *Journal of the American Chemical Society*, *80*(6), 1339. https://doi.org/10.1021/ja01539a017

**[27]** Dikin, D. A., Stankovich, S., Zimney, E. J., Piner, R. D., Dommett, G. H. B., Evmenenko, G., Nguyen, S. T., & Ruoff, R. S. (2007). Preparation and characterization of graphene oxide paper. *Nature*, *448*(7152), 457–460. https://doi.org/10.1038/nature06016

**[28]** Stankovich, S., Dikin, D. A., Piner, R. D., Kohlhaas, K. A., Kleinhammes, A., Jia, Y., Wu, Y., Nguyen, S. T., & Ruoff, R. S. (2007). Synthesis of graphene-based nanosheets via chemical reduction of exfoliated graphite oxide. *Carbon*, *45*(7), 1558–1565. https://doi.org/10.1016/j.carbon.2007.02.034

**[29]** Park, S., & Ruoff, R. S. (2009). Chemical methods for the production of graphenes. *Nature Nanotechnology*, *4*(4), 217–224. https://doi.org/10.1038/nnano.2009.58

**[30]** Dreyer, D. R., Park, S., Bielawski, C. W., & Ruoff, R. S. (2010). The chemistry of graphene oxide. *Chemical Society Reviews*, *39*(1), 228–240. https://doi.org/10.1039/b917103g

**[31]** Lerf, A., He, H., Forster, M., & Klinowski, J. (1998). Structure of graphite oxide revisited. *The Journal of Physical Chemistry B*, *102*(23), 4477–4482. https://doi.org/10.1021/jp9731821

**[32]** Szabó, T., Berkesi, O., Forgó, P., Josepovits, K., Sanakis, Y., Petridis, D., & Dékány, I. (2006). Evolution of surface functional groups in a series of progressively oxidized graphite oxides. *Chemistry of Materials*, *18*(11), 2740–2749. https://doi.org/10.1021/cm060258+

**[33]** He, H., Klinowski, J., Forster, M., & Lerf, A. (1998). A new structural model for graphite oxide. *Chemical Physics Letters*, *287*(1–2), 53–56. https://doi.org/10.1016/S0009-2614(98)00144-4

**[34]** Gao, W., Alemany, L. B., Ci, L., & Ajayan, P. M. (2009). New insights into the structure and reduction of graphite oxide. *Nature Chemistry*, *1*(5), 403–408. https://doi.org/10.1038/nchem.281

**[35]** Bagri, A., Mattevi, C., Acik, M., Chhowalla, M., & Shenoy, V. B. (2010). Structural evolution during the reduction of chemically derived graphene oxide. *Nature Chemistry*, *2*(7), 581–587. https://doi.org/10.1038/nchem.686

**[36]** Erickson, K., Erni, R., Lee, Z., Alem, N., Gannett, W., & Zettl, A. (2010). Determination of the local chemical structure of graphene oxide and reduced graphene oxide. *Advanced Materials*, *22*(40), 4467–4472. https://doi.org/10.1002/adma.201000732

**[37]** Mattevi, C., Eda, G., Agnoli, S., Miller, S., Mkhoyan, K. A., Celik, O., Mastrogiovanni, D., Granozzi, G., Garfunkel, E., & Chhowalla, M. (2009). Evolution of electrical, chemical, and structural properties of transparent and conducting chemically derived graphene thin films. *Advanced Functional Materials*, *19*(16), 2577–2583. https://doi.org/10.1002/adfm.200900166

**[38]** Eda, G., Fanchini, G., & Chhowalla, M. (2008). Large-area ultrathin films of reduced graphene oxide as a flexible and transparent conducting material. *Nature Nanotechnology*, *3*(5), 270–274. https://doi.org/10.1038/nnano.2008.83

**[39]** Gomez-Navarro, C., Weitz, R. T., Bittner, A. M., Scolari, M., Mews, A., Burghard, M., & Kern, K. (2007). Electronic transport properties of individual chemically reduced graphene oxide sheets. *Nano Letters*, *7*(11), 3499–3503. https://doi.org/10.1021/nl072090c

**[40]** Becerril, H. A., Mao, J., Liu, Z., Stoltenberg, R. M., Bao, Z., & Chen, Y. (2008). Evaluation of solution-processed reduced graphene oxide films as transparent conductors. *ACS Nano*, *2*(3), 463–470. https://doi.org/10.1021/nn700375n

**[41]** Li, D., Müller, M. B., Gilje, S., Kaner, R. B., & Wallace, G. G. (2008). Processable aqueous dispersions of graphene nanosheets. *Nature Nanotechnology*, *3*(2), 101–105. https://doi.org/10.1038/nnano.2007.451

**[42]** Si, Y., & Samulski, E. T. (2008). Synthesis of water soluble graphene. *Nano Letters*, *8*(6), 1679–1682. https://doi.org/10.1021/nl080604h

**[43]** Niyogi, S., Bekyarova, E., Itkis, M. E., McWilliams, J. L., Hamon, M. A., & Haddon, R. C. (2006). Solution properties of graphite and graphene. *Journal of the American Chemical Society*, *128*(24), 7720–7721. https://doi.org/10.1021/ja060680r

**[44]** Lomeda, J. R., Doyle, C. D., Kosynkin, D. V., Hwang, W. F., & Tour, J. M. (2008). Diazonium functionalization of surfactant-wrapped chemically converted graphene sheets. *Journal of the American Chemical Society*, *130*(48), 16201–16206. https://doi.org/10.1021/ja806499w

**[45]** Wang, X., Zhi, L., & Müllen, K. (2008). Transparent, conductive graphene electrodes for dye-sensitized solar cells. *Nano Letters*, *8*(1), 323–327. https://doi.org/10.1021/nl072838r

**[46]** Chmiola, J., Yushin, G., Gogotsi, Y., Portet, C., Simon, P., & Taberna, P. L. (2006). Anomalous increase in carbon capacitance at subnanometer pore sizes. *Science*, *313*(5794), 1760–1763. https://doi.org/10.1126/science.1132195

**[47]** Largeot, C., Portet, C., Chmiola, J., Taberna, P. L., Gogotsi, Y., & Simon, P. (2008). Relation between the ion size and pore size for an electric double-layer capacitor. *Journal of the American Chemical Society*, *130*(9), 2730–2731. https://doi.org/10.1021/ja7106178

**[48]** Kondrat, S., Perez, C. R., Presser, V., Gogotsi, Y., & Kornyshev, A. A. (2012). Effect of pore size and its dispersity on the energy storage in nanoporous supercapacitors. *Energy & Environmental Science*, *5*(4), 6474–6479. https://doi.org/10.1039/c2ee03092f

**[49]** Feng, G., Qiao, R., Huang, J., Dai, S., Sumpter, B. G., & Meunier, V. (2011). The importance of ion size and electrode curvature on electrical double layers in ionic liquids. *Physical Chemistry Chemical Physics*, *13*(3), 1152–1161. https://doi.org/10.1039/C0CP02077J

**[50]** Feng, G., Jiang, D. E., & Cummings, P. T. (2012). Curvature effect on the capacitance of electric double layers at ionic liquid/onion-like carbon interfaces. *Journal of Chemical Theory and Computation*, *8*(3), 1058–1063. https://doi.org/10.1021/ct200914j

**[51]** Huang, J., Sumpter, B. G., & Meunier, V. (2008). Theoretical model for nanoporous carbon supercapacitors. *Angewandte Chemie International Edition*, *47*(3), 520–524. https://doi.org/10.1002/anie.200703864

**[52]** Merlet, C., Rotenberg, B., Madden, P. A., Taberna, P. L., Simon, P., Gogotsi, Y., & Salanne, M. (2012). On the molecular origin of supercapacitance in nanoporous carbon electrodes. *Nature Materials*, *11*(4), 306–310. https://doi.org/10.1038/nmat3260

**[53]** Kornyshev, A. A. (2007). Double-layer in ionic liquids: Paradigm change? *The Journal of Physical Chemistry B*, *111*(20), 5545–5557. https://doi.org/10.1021/jp067857o

**[54]** Raymundo-Piñero, E., Kierzek, K., Machnikowski, J., & Béguin, F. (2006). Relationship between the nanoporous texture of activated carbons and their capacitance properties in different electrolytes. *Carbon*, *44*(12), 2498–2507. https://doi.org/10.1016/j.carbon.2006.05.022

**[55]** Armand, M., Endres, F., MacFarlane, D. R., Ohno, H., & Scrosati, B. (2009). Ionic-liquid materials for the electrochemical challenges of the future. *Nature Materials*, *8*(8), 621–629. https://doi.org/10.1038/nmat2448

**[56]** Kresge, C. T., Leonowicz, M. E., Roth, W. J., Vartuli, J. C., & Beck, J. S. (1992). Ordered mesoporous molecular sieves synthesized by a liquid-crystal template mechanism. *Nature*, *359*(6397), 710–712. https://doi.org/10.1038/359710a0

**[57]** Beck, J. S., Vartuli, J. C., Roth, W. J., Leonowicz, M. E., Kresge, C. T., Schmitt, K. D., Chu, C. T. W., Olson, D. H., Sheppard, E. W., McCullen, S. B., Higgins, J. B., & Schlenker, J. L. (1992). A new family of mesoporous molecular sieves prepared with liquid crystal templates. *Journal of the American Chemical Society*, *114*(27), 10834–10843. https://doi.org/10.1021/ja00053a020

**[58]** Zhao, D., Feng, J., Huo, Q., Melosh, N., Fredrickson, G. H., Chmelka, B. F., & Stucky, G. D. (1998). Triblock copolymer syntheses of mesoporous silica with periodic 50 to 300

angstrom pores. *Science*, *279*(5350), 548–552. https://doi.org/10.1126/science.279.5350.548

**[59]** Zhao, D., Huo, Q., Feng, J., Chmelka, B. F., & Stucky, G. D. (1998). Nonionic triblock and star diblock copolymer and oligomeric surfactant syntheses of highly ordered, hydrothermally stable, mesoporous silica structures. *Journal of the American Chemical Society*, *120*(24), 6024–6036. https://doi.org/10.1021/ja974025i

**[60]** Ryoo, R., Joo, S. H., & Jun, S. (1999). Synthesis of highly ordered carbon molecular sieves via template-mediated structural transformation. *The Journal of Physical Chemistry B*, *103*(37), 7743–7746. https://doi.org/10.1021/jp991673a

**[61]** Jun, S., Joo, S. H., Ryoo, R., Kruk, M., Jaroniec, M., Liu, Z., Ohsuna, T., & Terasaki, O. (2000). Synthesis of new, nanoporous carbon with hexagonally ordered mesostructure. *Journal of the American Chemical Society*, *122*(43), 10712–10713. https://doi.org/10.1021/ja002261e

**[62]** Stöber, W., Fink, A., & Bohn, E. (1968). Controlled growth of monodisperse silica spheres in the micron size range. *Journal of Colloid and Interface Science*, *26*(1), 62–69. https://doi.org/10.1016/0021-9797(68)90272-5

**[63]** Liang, C., Li, Z., & Dai, S. (2008). Mesoporous carbon materials: Synthesis and modification. *Angewandte Chemie International Edition*, *47*(20), 3696–3717. https://doi.org/10.1002/anie.200702046

**[64]** Lee, J., Kim, J., & Hyeon, T. (2006). Recent progress in the synthesis of porous carbon materials. *Advanced Materials*, *18*(16), 2073–2094. https://doi.org/10.1002/adma.200501576

**[65]** Lei, Z., Christov, N., & Zhao, X. S. (2011). Intercalation of mesoporous carbon spheres between reduced graphene oxide sheets for preparing high-rate supercapacitor electrodes. *Energy & Environmental Science*, *4*(5), 1866–1873. https://doi.org/10.1039/C1EE01094H

**[66]** Xu, Y., Lin, Z., Zhong, X., Huang, X., Weiss, N. O., Huang, Y., & Duan, X. (2014). Holey graphene frameworks for highly efficient capacitive energy storage. *Nature Communications*, *5*, Article 4554. https://doi.org/10.1038/ncomms5554

**[67]** Xu, Y., Lin, Z., Huang, X., Liu, Y., Huang, Y., & Duan, X. (2013). Flexible solid-state supercapacitors based on three-dimensional graphene hydrogel films. *ACS Nano*, *7*(5), 4042–4049. https://doi.org/10.1021/nn4000836

**[68]** Xu, Y., Sheng, K., Li, C., & Shi, G. (2010). Self-assembled graphene hydrogel via a one-step hydrothermal process. *ACS Nano*, *4*(7), 4324–4330. https://doi.org/10.1021/nn101187z

**[69]** Wu, Z. S., Sun, Y., Tan, Y. Z., Yang, S., Feng, X., & Müllen, K. (2012). Three-dimensional graphene-based macro- and mesoporous frameworks for high-performance electrochemical capacitors. *Journal of the American Chemical Society*, *134*(47), 19532–19535. https://doi.org/10.1021/ja308676h

**[70]** Choi, B. G., Yang, M., Hong, W. H., Choi, J. W., & Huh, Y. S. (2012). 3D macroporous graphene frameworks for supercapacitors with high energy and power densities. *ACS Nano*, *6*(5), 4020–4028. https://doi.org/10.1021/nn3003345

**[71]** Wu, Z. S., Ren, W., Wang, D. W., Li, F., Liu, B., & Cheng, H. M. (2010). High-energy $MnO_2$ nanowire/graphene and graphene asymmetric electrochemical capacitors. *ACS Nano*, *4*(10), 5835–5842. https://doi.org/10.1021/nn101754k

**[72]** Yan, J., Fan, Z., Wei, T., Qian, W., Zhang, M., & Wei, F. (2010). Fast and reversible surface redox reaction of graphene-$MnO_2$ composites as supercapacitor electrodes. *Carbon*, *48*(13), 3825–3833. https://doi.org/10.1016/j.carbon.2010.06.047

**[73]** Fan, Z., Yan, J., Wei, T., Zhi, L., Ning, G., Li, T., & Wei, F. (2011). Asymmetric supercapacitors based on graphene/$MnO_2$ and activated carbon nanofiber electrodes with high power and energy density. *Advanced Functional Materials*, *21*(12), 2366–2375. https://doi.org/10.1002/adfm.201100058

**[74]** Inagaki, M., Toyoda, M., Soneda, Y., & Morishita, T. (2018). Nitrogen-doped carbon materials. *Carbon*, *132*, 104–140. https://doi.org/10.1016/j.carbon.2018.02.024

**[75]** Wu, Z. S., Winter, A., Chen, L., Sun, Y., Turchanin, A., Feng, X., & Müllen, K. (2012). Three-dimensional nitrogen and boron co-doped graphene for high-performance all-solid-state supercapacitors. *Advanced Materials*, *24*(37), 5130–5135. https://doi.org/10.1002/adma.201201948

**[76]** Zhao, Y., Hu, C., Hu, Y., Cheng, H., Shi, G., & Qu, L. (2012). A versatile, ultralight, nitrogen-doped graphene framework. *Angewandte Chemie International Edition*, *51*(45), 11371–11375. https://doi.org/10.1002/anie.201206554

**[77]** Han, J., Zhang, L. L., Lee, S., Oh, J., Lee, K. S., Potts, J. R., Ji, J., Zhao, X., Ruoff, R. S., & Park, S. (2013). Generation of B-doped graphene nanoplatelets using a solution process and their supercapacitor applications. *ACS Nano*, *7*(1), 19–26. https://doi.org/10.1021/nn305417x

**[78]** Sheng, Z. H., Shao, L., Chen, J. J., Bao, W. J., Wang, F. B., & Xia, X. H. (2011). Catalyst-free synthesis of nitrogen-doped graphene via thermal annealing graphite oxide with melamine and its excellent electrocatalysis. *ACS Nano*, *5*(6), 4350–4358. https://doi.org/10.1021/nn103584t

**[79]** Wang, X., Li, X., Zhang, L., Yoon, Y., Weber, P. K., Wang, X., Guo, J., & Dai, H. (2009). N-doping of graphene through electrothermal reactions with ammonia. *Science*, *324*(5928), 768–771. https://doi.org/10.1126/science.1170335

**[80]** Qu, L., Liu, Y., Baek, J. B., & Dai, L. (2010). Nitrogen-doped graphene as efficient metal-free electrocatalyst for oxygen reduction in fuel cells.

*ACS Nano*, *4*(3), 1321–1326. https://doi.org/10.1021/nn901850u

**[81]** Geng, D., Yang, S., Zhang, Y., Yang, J., Liu, J., Li, R., Sham, T. K., & Sun, X. (2011). Nitrogen doping effects on the structure and morphology of graphene. *Applied Surface Science*, *257*(22), 9193–9198. https://doi.org/10.1016/j.apsusc.2011.05.131

**[82]** Panchakarla, L. S., Subrahmanyam, K. S., Saha, S. K., Govindaraj, A., Krishnamurthy, H. R., Waghmare, U. V., & Rao, C. N. R. (2009). Synthesis, structure, and properties of boron- and nitrogen-doped graphenes. *Advanced Materials*, *21*(46), 4726–4730. https://doi.org/10.1002/adma.200901285

**[83]** Wang, H., Maiyalagan, T., & Wang, X. (2012). Review on recent progress in nitrogen-doped graphene: Synthesis, characterization, and its potential applications. *ACS Catalysis*, *2*(5), 781–794. https://doi.org/10.1021/cs200652y

**[84]** Parvez, K., Yang, S., Hernandez, Y., Winter, A., Turchanin, A., Feng, X., & Müllen, K. (2012). Nitrogen-doped graphene and its iron-based composite as efficient electrocatalysts for oxygen reduction reaction. *ACS Nano*, *6*(11), 9541–9550. https://doi.org/10.1021/nn302674q

**[85]** Zhao, L., He, R., Rim, K. T., Schiros, T., Kim, K. S., Zhou, H., Gutiérrez, C., Chockalingam, S. P., Arguello, C. J., Pálová, L., Nordlund, D., Hybertsen, M. S., Reichman, D. R., Heinz, T. F., Kim, P., Pinczuk, A., Flynn, G. W., & Pasupathy, A. N. (2011). Visualizing individual nitrogen dopants in monolayer graphene. *Science*, *333*(6045), 999–1003. https://doi.org/10.1126/science.1208759

**[86]** Lv, R., Li, Q., Botello-Méndez, A. R., Hayashi, T., Wang, B., Berkdemir, A., Hao, Q., Elías, A. L., Cruz-Silva, R., Gutiérrez, H. R., Kim, Y. A., Muramatsu, H., Zhu, J., Endo, M., Terrones, H., Charlier, J.-C., Pan, M., & Terrones, M. (2012). Nitrogen-doped graphene: Beyond single substitution and enhanced molecular sensing. *Scientific Reports*, *2*, Article 586. https://doi.org/10.1038/srep00586

**[87]** Lin, T., Chen, I. W., Liu, F., Yang, C., Bi, H., Xu, F., & Huang, F. (2015). Nitrogen-doped mesoporous carbon of extraordinary capacitance for electrochemical energy storage. *Science*, *350*(6267), 1508–1513. https://doi.org/10.1126/science.aab3798

**[88]** Pech, D., Brunet, M., Durou, H., Huang, P., Mochalin, V., Gogotsi, Y., Taberna, P. L., & Simon, P. (2010). Ultrahigh-power micrometre-sized supercapacitors based on onion-like carbon. *Nature Nanotechnology*, *5*(9), 651–654. https://doi.org/10.1038/nnano.2010.162

**[89]** Huang, P., Heon, M., Pech, D., Brunet, M., Taberna, P. L., Gogotsi, Y., Lofland, S., Hettinger, J. D., & Simon, P. (2013). Micro-supercapacitors from carbide derived carbon (CDC) films on silicon chips. *Journal of Power Sources*, *225*, 240–244. https://doi.org/10.1016/j.jpowsour.2012.10.020

**[90]** Liu, C., Yu, Z., Neff, D., Zhamu, A., & Jang, B. Z. (2010). Graphene-based supercapacitor with an ultrahigh energy density. *Nano Letters*, *10*(12), 4863–4868. https://doi.org/10.1021/nl102661q

**[91]** Brunauer, S., Emmett, P. H., & Teller, E. (1938). Adsorption of gases in multimolecular layers. *Journal of the American Chemical Society*, *60*(2), 309–319. https://doi.org/10.1021/ja01269a023

**[92]** Barrett, E. P., Joyner, L. G., & Halenda, P. P. (1951). The determination of pore volume and area distributions in porous substances. I. Computations from nitrogen isotherms. *Journal of the American Chemical Society*, *73*(1), 373–380. https://doi.org/10.1021/ja01145a126

**[93]** Landers, J., Gor, G. Y., & Neimark, A. V. (2013). Density functional theory methods for characterization of porous materials. *Colloids and Surfaces A: Physicochemical and Engineering Aspects*, *437*, 3–32. https://doi.org/10.1016/j.colsurfa.2013.01.007

**[94]** Thommes, M., Kaneko, K., Neimark, A. V., Olivier, J. P., Rodriguez-Reinoso, F., Rouquerol, J., & Sing, K. S. W. (2015). Physisorption of gases, with special reference to the evaluation of surface area and pore size distribution (IUPAC technical report). *Pure and Applied Chemistry*, *87*(9–10), 1051–1069. https://doi.org/10.1515/pac-2014-1117

**[95]** Rouquerol, J., Avnir, D., Fairbridge, C. W., Everett, D. H., Haynes, J. H., Pernicone, N., Ramsay, J. D. F., Sing, K. S. W., & Unger, K. K. (1994). Recommendations for the characterization of porous solids. *Pure and Applied Chemistry*, *66*(8), 1739–1758. https://doi.org/10.1351/pac199466081739

**[96]** Sing, K. S. W. (1985). Reporting physisorption data for gas/solid systems with special reference to the determination of surface area and porosity. *Pure and Applied Chemistry*, *57*(4), 603–619. https://doi.org/10.1351/pac198557040603

**[97]** Ferrari, A. C., & Robertson, J. (2000). Interpretation of Raman spectra of disordered and amorphous carbon. *Physical Review B*, *61*(20), 14095–14107. https://doi.org/10.1103/PhysRevB.61.14095

**[98]** Ferrari, A. C., Meyer, J. C., Scardaci, V., Casiraghi, C., Lazzeri, M., Mauri, F., Piscanec, S., Jiang, D., Novoselov, K. S., Roth, S., & Geim, A. K. (2006). Raman spectrum of graphene and graphene layers. *Physical Review Letters*, *97*(18), Article 187401. https://doi.org/10.1103/PhysRevLett.97.187401

**[99]** Tuinstra, F., & Koenig, J. L. (1970). Raman spectrum of graphite. *The Journal of Chemical Physics*, *53*(3), 1126–1130. https://doi.org/10.1063/1.1674108

**[100]** Ferrari, A. C., & Basko, D. M. (2013). Raman spectroscopy as a versatile tool for studying the properties of graphene. *Nature Nanotechnology*,

*8*(4), 235–246. https://doi.org/10.1038/nnano.2013.46

**[101]** Malard, L. M., Pimenta, M. A., Dresselhaus, G., & Dresselhaus, M. S. (2009). Raman spectroscopy in graphene. *Physics Reports*, *473*(5–6), 51–87. https://doi.org/10.1016/j.physrep.2009.02.003

**[102]** Gogotsi, Y., & Simon, P. (2011). True performance metrics in electrochemical energy storage. *Science*, *334*(6058), 917–918. https://doi.org/10.1126/science.1213003

**[103]** Stoller, M. D., & Ruoff, R. S. (2010). Best practice methods for determining an electrode material's performance for ultracapacitors. *Energy & Environmental Science*, *3*(9), 1294–1301. https://doi.org/10.1039/C0EE00074D

**[104]** Cançado, L. G., Jorio, A., Ferreira, E. H. M., Stavale, F., Achete, C. A., Capaz, R. B., Moutinho, M. V. O., Lombardo, A., Kulmala, T. S., & Ferrari, A. C. (2011). Quantifying defects in graphene via Raman spectroscopy at different excitation energies. *Nano Letters*, *11*(8), 3190–3196. https://doi.org/10.1021/nl201432g

**[105]** Yang, D., Velamakanni, A., Bozoklu, G., Park, S., Stoller, M., Piner, R. D., Stankovich, S., Jung, I., Field, D. A., Ventrice, C. A., & Ruoff, R. S. (2009). Chemical analysis of graphene oxide films after heat and chemical treatments by X-ray photoelectron and micro-Raman spectroscopy. *Carbon*, *47*(1), 145–152. https://doi.org/10.1016/j.carbon.2008.09.045

**[106]** Taberna, P. L., Simon, P., & Fauvarque, J. F. (2003). Electrochemical characteristics and impedance spectroscopy studies of carbon-carbon supercapacitors. *Journal of The Electrochemical Society*, *150*(3), A292–A300. https://doi.org/10.1149/1.1543948